

# Population balance modeling of InP formation in an automated synthesis platform

Zhuang Wang <sup>a</sup>, Nabi E. Traoré <sup>b, c</sup>, Tobias Schikarski <sup>b, c</sup>, Lisa Stiegler <sup>b, c</sup>, Dominik Drobek <sup>d</sup>, Benjamin Apeleo Zubiri <sup>d</sup>, Erdmann Spiecker <sup>d</sup>, Johannes Walter <sup>b, c</sup>, Wolfgang Peukert <sup>b, c</sup>, Lukas Pflug <sup>e, \*</sup>, Doris Segets <sup>a, f, \*</sup>

<sup>a</sup> Institute for Energy and Materials Processes (EMPI), University of Duisburg-Essen, Duisburg, Germany

<sup>b</sup> Institute of Particle Technology, Friedrich-Alexander-Universität Erlangen-Nürnberg (FAU), Erlangen, Germany

<sup>c</sup> Interdisciplinary Center for Functional Particle Systems (FPS), Friedrich-Alexander-Universität Erlangen-Nürnberg (FAU), Erlangen, Germany

<sup>d</sup> Institute of Micro- and Nanostructure Research (IMN) & Center for Nanoanalysis and Electron Microscopy (CENEM), Interdisciplinary Center for Nanostructured Films (IZNF), Friedrich-Alexander-Universität Erlangen-Nürnberg (FAU), Erlangen, Germany

<sup>e</sup> Competence Unit for Scientific Computing (CSC), Friedrich-Alexander-Universität Erlangen-Nürnberg (FAU), Erlangen, Germany

<sup>f</sup> Center for Nanointegration Duisburg-Essen (CENIDE), Duisburg, Germany

\* Corresponding authors: [doris.segets@uni-due.de](mailto:doris.segets@uni-due.de), [lukas.pflug@fau.de](mailto:lukas.pflug@fau.de)

**Key words:** InP, automated synthesis, population balance equation, simulation

## Abstract

Despite great progress in the synthetic chemistry of InP QDs, a predictive model to describe their temporal formation is still missing. In this work, we introduce a population balance model incorporating liquid phase reactions, homogeneous nucleation and reaction-limited growth of InP supported with the highly reproducible and reliable experimental data acquired from an automated robotic synthesis platform. A comparison between experimental kinetic data (different initial concentrations and temperatures) and simulations was made. The proposed model describes the temporal evolution of solid concentration, particle diameter and particle size distribution very well. The quantitative agreement between experiments and simulations was only achieved by global optimization to identify unknown and hardly measurable material parameters and kinetic constants such as surface energy, growth rate constants or activation energies. We see this model rendering the first step towards the development of more refined models that enable rigorous optimization and control of the production process for III-V semiconductors.

## 1. Introduction

Semiconductor nanocrystals, namely quantum dots (QDs), have received tremendous attention from the scientific community in the past few decades because of their size dependent optical and electronic properties which result from the quantum confinement effect [1]. These unique optical and electronic properties make them find use in many applications, including light emitting diodes (LEDs) [2, 3], solar cells [4, 5] and in vivo bioimaging [6, 7]. Since the pioneering works from Ekimov [8] and Brus [9], Cadmium (Cd) and Lead (Pb) based II–VI and IV–VI group compounds have been the most widely investigated compositions of QDs which exhibit narrow particle size distributions (PSDs) and high photoluminescence quantum yields (PLQY) approaching unity [1, 10]. However, the heavy metal elements associated with these QDs raise concerns about the toxicity which is a major obstacle for clinical and industrial applications. This brings up the need for less toxic and more environmentally friendly replacements.

Indium phosphide (InP) QDs featuring low toxicity and comparable optical properties have attracted a lot of attention as one of the most promising replacements for their Cd/Pb-based counterparts. Over the past few decades, much work has been devoted to developing chemistries and processes for the preparation of high quality InP QDs [11, 12]. Hot injection in a three-neck flask is the most typical lab-scale technique for the synthesis of QDs which however inherently comes with disadvantages, i.e., ill-defined mixing and poor batch-to-batch reproducibility [13]. Automated synthesis platforms have been successfully deployed to significantly improve the reproducibility of syntheses. Salley et al. utilized a modular robotic platform for the synthesis of polyoxometalates [14], while Chan et al. and Salaheldin et al. showed a highly reproducible synthesis of CdSe QDs [15, 16]. The excellent reproducibility, which is achieved by the categorical removal of the human factor, not only increases the reliability of the final product, but also enables higher throughput by automated cleaning [17] and improved understanding due to concise and reproducible sampling processes, even at early stages during fast syntheses.

In order to gain a better understanding of the formation mechanism and further control over the particle size and PSD of InP QDs, studies on the underlying reaction kinetics and the formation mechanism were widely reported. Similar to II-VI QDs like CdSe, in the case of InP, the precursor conversion rate was expected to help control the size of the particles and minimize dispersity. However and contrary to other QD materials [18-20], Bawendi et al. [21] demonstrated that in case of InP QDs the experimentally found particle size did not match with the expectations, and that a reduced concentration of reactive precursors did not yield the expected narrowing of the PSD. Recently, the same group developed a seedless continuous injection strategy that enables the

growth of large InP QDs and simultaneously maintains a low dispersity [22]. They also reported that the nucleation rate depends on the concentration of intermediates and that the growth rate depends on the size of the QDs. Dubertret et al. [23] studied the formation kinetics of InP QDs synthesized using aminophosphine and suggested that under certain conditions the growth of InP QDs approaches a LaMer-type growth [24]. However, a recent mechanistic study suggested that the formation of InP does not follow this model [25] and that it is the temperature that dictates the relationship of nucleation and growth. I.e., at low temperature (e.g. 180 °C) nucleation and growth are concurrent throughout the reaction. For the recently emerging aminophosphine-based synthesis of InP QDs that avoids toxic and explosive tris(trimethylsilyl)phosphine (PTMS) as P-source, Hens et al. [26] investigated the role of aminophosphine. They found that aminophosphine acts as both the precursor and the reducing agent, while the chemical yield of InP formation agrees with  $4 P(+III) \rightarrow P(-III) + 3 P(+V)$ , where P represents the phosphorus-containing reactant and product. During the formation of InP, magic sized clusters were also found as a key intermediate [27]. So far this has only been reported for the PTMS-based synthesis [28]. Despite tremendous experimental efforts in the development of synthetic chemistry, optimization and control of InP QDs, production processes still follow a trial-and-error approach, that requires a huge number of laboratory experiments to find optimal reaction conditions to yield desired sizes and size distributions. Hence there is a general need to develop predictive models that enable the targeted synthesis of InP QDs with desired properties. To the best of our knowledge, such a model, featuring careful investigation of nanoparticles dispersity and solid concentration as a function of the reaction conditions and time, has not been presented yet.

In this work, we present a predictive population balance model that enables a quantitative description of the temporal evolution of solid concentration and particle size distribution for a synthesis of InP QDs based on the aminophosphine-route. The unknown variables, i.e., reaction rate constants, growth rate constant, surface energy, and equilibrium solubility were calibrated based on kinetic data. I.e., the evolution of mean particle size and solid concentration over time as well as the respective final PSDs were analyzed for a range of temperatures. An excellent agreement between experiments and simulations was found. Noteworthy, not only the predicted temporal evolution of solid concentration and particle size distribution matched our experimental data well, but the derived rate constants followed an Arrhenius-type behavior with reasonable activation energy, evidencing plausibility of our model and the derived parameters.

## 2. Experimental and methods

### 2.1 Chemicals

Indium chloride ( $\text{InCl}_3$ , 99.999 %) and tris(dimethylamino)phosphine (PDMA, 97 %) were purchased from Sigma-Aldrich. Oleylamine (OLA, 80-90 %) and 1-Octadecene (ODE, 90 %) were purchased from Acros Organics. Ethanol (analytical grade) and n-hexane ( $\geq 99$  %) were purchased from VWR Chemicals. All chemicals were used without further purification.

### 2.2 Automated synthesis of InP QDs

A Swing XL Autoplant II hybrid platform from Chemspeed© Technologies was used for all syntheses. The whole system was encapsulated in a glovebox (MBraun) under nitrogen atmosphere ( $\text{O}_2$  and  $\text{H}_2\text{O} < 20$  ppm). Post-processing steps, which were carried out under inert atmosphere were also performed within this glovebox. Components of the robotic setup that are relevant for the process shown in this work include a liquid handling tool (4 needle head – 4NH) and a stirred tank reactor (STR) module made of stainless steel. The 4NH, which is connected to four glass syringe pumps, handles liquids with high accuracy (relative standard deviation (RSD) = 1.5 %) and is capable of handling up to four different liquids simultaneously. To avoid cross contamination, the 4NH is capable of cleaning itself in between sampling using ODE as the system liquid. The reactor module consists of six independent stirred tank reactors with an operating volume of 80 mL. The reactors can be heated via a heating jacket to up to 280 °C and are equipped with hollow shaft triple blade stirrers. This accounts for unprecedented mixing control compared to the magnetic stirrer bars applied at the lab scale. More details on the robotic system can be found in our previous publication [15].

In a typical synthesis run, firstly, 309.6 mg of  $\text{InCl}_3$  was added manually into one of the STRs. Then the automated workflow was started. The reactor was loaded with 8 mL of ODE and 12 mL of OLA by the 4NH, while self-cleaning after each dispense. Afterwards, the reactor was heated to 150 °C while being stirred at 100 rpm. The temperature was held for 1.5 h in order to fully dissolve  $\text{InCl}_3$  in the solvent, evaporate potentially dissolved water and stabilize the temperature. After this period, the reactor was heated to the reaction temperature (160-200 °C), the stirrer speed was increased to 600 rpm and after reliably reaching the set temperature, 0.5 mL of PDMA was rapidly injected into the hot precursor solution. Upon the injection of PDMA, supersaturation was generated where the InP QDs formed by nucleation and growth. To track the formation of InP QDs inside the reactor vessel, samples (150  $\mu\text{L}$ ) were taken via the 4NH at 20 s, 50 s, 1.5 min, 6 min, 7 min, 8 min, 13 min, 15 min, 20 min, 25 min, 30 min and 40 min after the injection and stored in a polystyrene 96-well micro titer plate. After the automated synthesis protocol was

complete, each aliquot was manually transferred into a centrifuge tube, flocculated with ethanol, centrifuged at 10000 rpm for 20 min under N<sub>2</sub> atmosphere and redispersed in n-hexane for further characterization.

### 2.3 Characterizations

X-ray diffraction (XRD) measurements were performed using a powder diffractometer in a Bragg-Brentano setup (Empyrean, Malvern Panalytical, United Kingdom). The device was equipped with a GaliPIX<sup>3D</sup> detector. All patterns were recorded via Cu K $\alpha$  radiation ( $\lambda = 0.15405$  nm) in the 2-theta range of 10 to 80°. Prior to analysis, the InP QDs were dried on a silicon zero background holder under nitrogen atmosphere.

Scanning transmission electron microscopy (STEM) images were taken in a Thermo Fisher Scientific Spectra 200 C-FEG microscope operated in STEM mode using a high-angle annular dark-field (HAADF) detector (collection-angle ranging from 56-200 mrad) with an acceleration voltage of 200 kV. Before, the QDs were dried on a 200-mesh carbon-coated copper TEM grid (Plano GmbH) under nitrogen atmosphere and subsequently cleaned in a plasma cleaner (Fischione Instruments Model 1070 NanoClean) with Argon plasma.

UV-visible measurements (UV-vis) were performed via a Varian Cary 100 spectrometer with a wavelength range of 200 – 800 nm and a spectral resolution of 1 nm. A background correction was performed based on the solvent within the QD dispersion (n-hexane). Quartz glass cuvettes with an optical path length of 1 cm were used for the measurements. Prior to each measurement, the QDs were diluted by additional n-hexane to achieve a maximum extinction of the first excitonic peak below unity and thus to be in the linear range of Lambert-Beer's law.

Analytical ultracentrifugation (AUC) experiments were conducted with a preparative ultracentrifuge from Beckman Coulter, type Optima L-90K, equipped with a mirror-based multiwavelength extinction detector from Nanolytics Instruments. Further details about the instrument and the method can be found in previous work [29, 30]. For sample preparation, InP QD dispersions in n-hexane of different ripening times were diluted to end up with an optical density of around 0.8 within a wavelength range between 400 nm and 575 nm, measured at a path length of 10 mm. Prior to each measurement, the QD dispersions were treated in an ultrasonic bath for 15 minutes. 400  $\mu$ L of each sample was filled into measuring cells from Nanolytics Instruments equipped with a two-sector titanium centerpiece with an optical path length of 12 mm. The measurements were conducted at a rotor speed of 10000 rpm while the temperature was kept constant at 20 °C.

All sedimentation data were analyzed at a wavelength between 400 nm and 575 nm, to have an optical density close to unity which guaranteed good signal within the Lambert-Beer region. Data evaluation was carried out using the SEDFIT software (version 16.1c) using the continuous sedimentation  $c(s)$  method which corrects for diffusional broadening of the sedimentation boundaries [31]. During analysis, the frictional ratio was set to unity and the partial specific volume was treated as a floating parameter. The meniscus, time and radial invariant noise were fitted. The density and viscosity of the solvent were 0.6596 g/cm<sup>3</sup> and 0.313 mPa · s, respectively. For each sample, the full diffusion-corrected sedimentation coefficient distributions and mean partial specific volumes were obtained. It needs to be noted that the best-fit partial specific volumes have no practical implications here as the exact frictional ratio remains unknown due to the non-spherical shape of the QDs.

## 2.4 Particle size distribution and solid concentration

Particle size distributions (PSDs) and solid concentrations ( $C_s$ ) were derived from UV-vis spectra [15]. The framework for the interpretation of UV-vis data into PSDs was originally published by Segets et al. [32, 33]. Noteworthy, the particle size derived from the UV-vis spectra specifically refers to the volume-equivalent diameter of the particles. In order to apply it to InP QDs, a bulk band gap energy of 1.35 eV was adopted and the size-dependent band gap energy was derived from literature data [34-41]. The solid concentration was calculated based on a previous report from Tessier et al. [12]:

$$C_{InP} = \frac{A_{413} \ln 10}{\frac{u_{i,413} L}{V_M}} d \quad (1)$$

Here,  $A_{413}$  is the measured absorbance for the QD aliquots in n-hexane at 413 nm,  $u_{i,413}$  is the intrinsic absorption coefficient at 413 nm,  $L$  is the optical path length of light,  $V_M$  is the molar volume and  $d$  is the dilution factor.

## 3 Results and discussion

### 3.1 Automated synthesis and reproducibility

Prior to discussing the underlying mechanism and the proposed model of InP formation, it is essential to first elucidate on the automated robot synthesis platform that enabled accurate tracking of the InP QD formation. Fig. 1a shows a schematic of a stirred tank reactor used for the synthesis of the QDs. QD synthesis has been first reported within this setup for CdSe QDs by Salaheldin et al. [15]. As briefly mentioned in Section 2.2, the formation of InP QDs takes place in the reactor at high temperatures (160-200 °C) with In and P precursors undergoing a

conversion, nucleation and growth step to form InP QDs. In this work, aminophosphine was used as P precursor, for which it is reported that it will undergo transamination with oleylamine and a subsequent disproportionation reaction during the precursor conversion [26]. As shown in Fig. 1b, the XRD pattern of as-synthesized InP QDs was in good agreement with the zinc blende structure, indicating the successful InP formation. As expected, peak broadening due to the small size of the InP nanocrystals was observed. Additionally, in order to ensure the reproducibility of our robotic synthesis platform, different batches were produced at different times and in different STRs of the reactor module. Fig. 1c shows the UV-vis spectra of InP QDs synthesized at different reaction times showing good agreement of two batches (see also the comparison of two batches in different reactors in Fig. S1). These results indicate a good reproducibility of the InP synthesis in the robotic platform which therefore enables the acquisition of kinetic data with sufficient accuracy that it can be used as trustworthy input for population balance modelling.

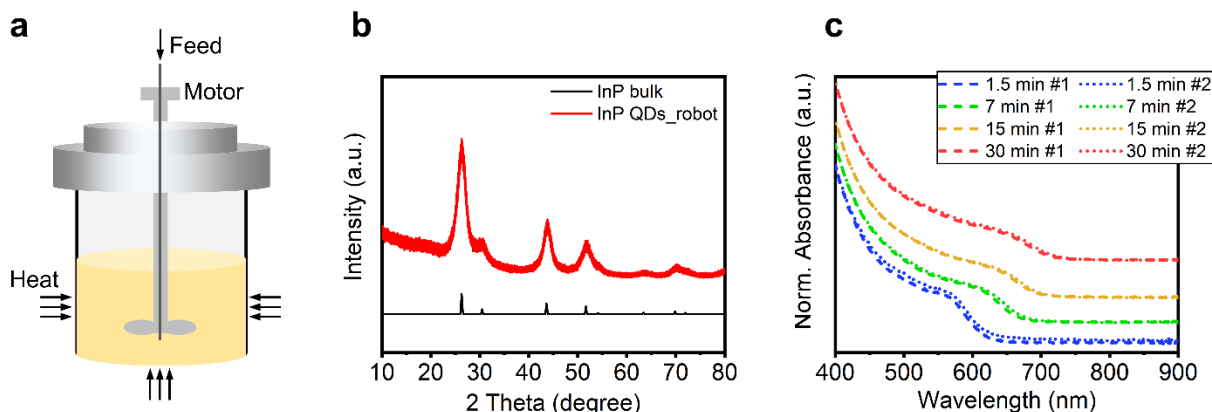


**Fig. 1.** a) Schematic of the stirred tank reactor module of the automated synthesis platform; b) XRD patterns of as-synthesized InP QDs and InP bulk as reference; c) Absorbance spectra of synthesized InP QDs taken at different time points throughout multiple reactions in n-hexane to demonstrate the reproducibility of the synthesis.

### 3.2 InP formation: Size characterization

In order to characterize the PSD that determines the optical properties of InP QDs, UV-vis spectroscopy, and STEM analysis were performed. Fig. 2a and Fig. 2b show the UV-vis spectra and the therefrom-derived PSDs at different reaction times during the InP formation. The absorption peaks shift from 512 nm to 628 nm as the reaction time increases, which indicates the growth of InP QDs over time. Noteworthy, while being the highest in the beginning of the reaction where the supersaturation is the highest, for higher reaction times the growth rate slows down. The particle size ( $x_{mod}$ ) results, shown in Fig. 2b, suggest that InP QDs grow from 2.4 nm to 3.5 nm in the first 15 mins and in the second 15 mins only from 3.5 nm to 3.8 nm. Fig. 2c illustrates

the relation between the first excitonic peak and the volume-equivalent size of spherical and tetrahedral InP QDs. The coincidence strongly indicates that the band gap corresponds to the equivalent sphere with semiconducting volume regardless of shape (Fig. 2c, [42]). I.e., the PSDs derived from the UV-vis spectra can be interpreted as volume equivalent diameters, even in the case of InP QDs with tetrahedral shape.

In addition to the PSDs derived from UV-vis, we also obtained PSDs from STEM image analysis and compared both distributions. Exemplarily, a STEM image of an InP aliquot taken at 30 min is shown in Fig. 2d. From the STEM image, a tetrahedral shape of the as-synthesized InP QDs was observed which was also reported in previous studies involving aminophosphine-based syntheses [42, 43]. The volume equivalent diameters were calculated based on the observed tetrahedral shape in the STEM and the comparison between the PSD from UV-vis and the PSD from STEM is shown in Fig. 2e. It can be seen that for InP aliquots isolated at a reaction time of 30 min, the PSD from STEM shows a good agreement with the PSD calculated from UV-vis. In line with our previous study [33], this further confirms that the PSD from UV-vis can be applied to track the evolution of the particle size distribution of equivalent volume over the course of InP synthesis. In combination with the accurate sampling times that are achieved by automation, this opens the possibility of a fast and reliable characterization of the InP QDs via their optical properties.

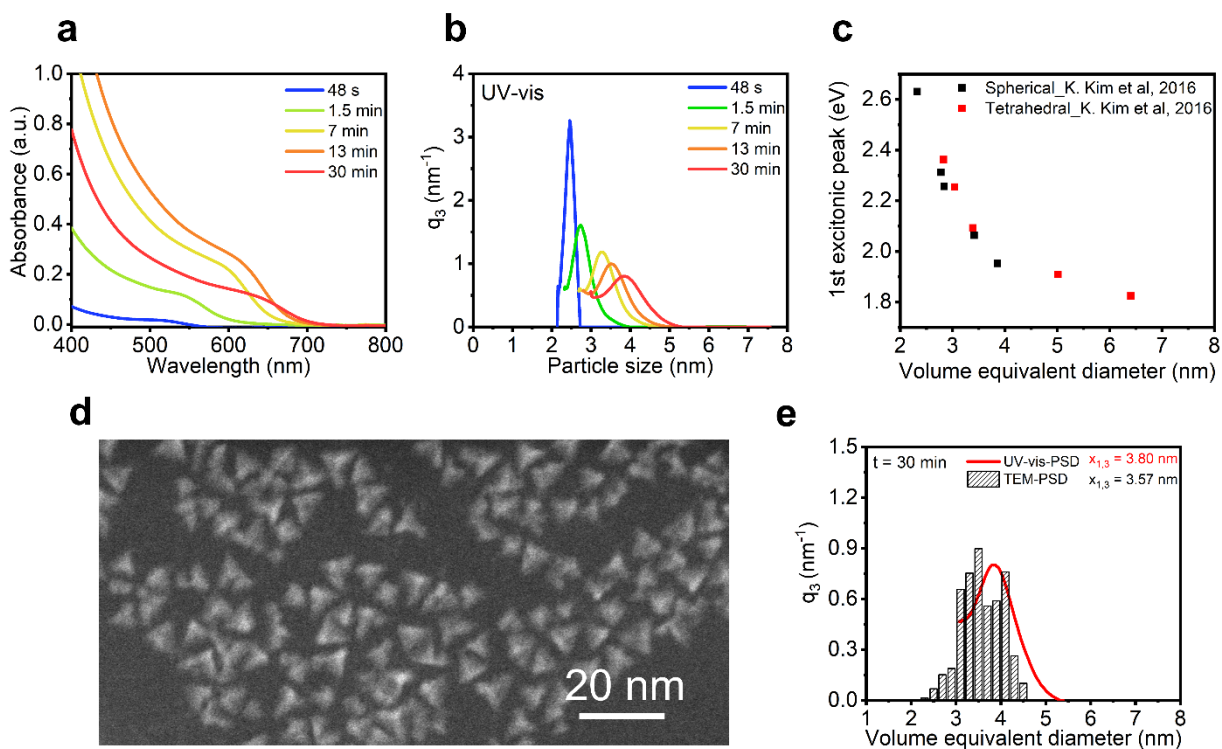


**Fig. 2.** a) UV-vis spectra of InP QDs derived from aliquots isolated at different reaction times during InP QD formation; b) PSDs derived from UV-vis spectra; c) position of the first excitonic peak as a function of the sphere equivalent QD size for tetrahedral and spherical QDs [42]; d) STEM image of InP QDs at 30 min and e) comparison between the PSD derived from UV-vis measurements and the PSD derived from STEM analysis (110 particles counted) shown as histogram.

Besides STEM and the deconvolution of UV-vis data, the InP QD formation was also investigated by AUC. The sedimentation coefficient distributions of the QDs formed within a time scale of 48 s to 30 min increase due to the growing side lengths of the tetrapods/tetrahedrons and with this the increasing mass of the QDs (Fig. 3). When neglecting the non-sphericity of the particles for the calculation of the PSD from the sedimentation coefficient distribution, a clear size mismatch can be recognized when comparing it to the results of the UV-vis analysis, which is especially notable at longer synthesis times (see Fig. S2). Due to this, we considered the tetrahedral shape of the particles when calculating the volume equivalent diameters from the sedimentation coefficient distribution (results shown in Fig. S3 in the supporting information for a selected sample at 30 min). However, this consideration led to an even more pronounced mismatch in the final PSDs because of the increased volume-specific surface of the tetrapods, which would result in an even smaller effective sedimentation coefficient due to the density effect of the ligand.

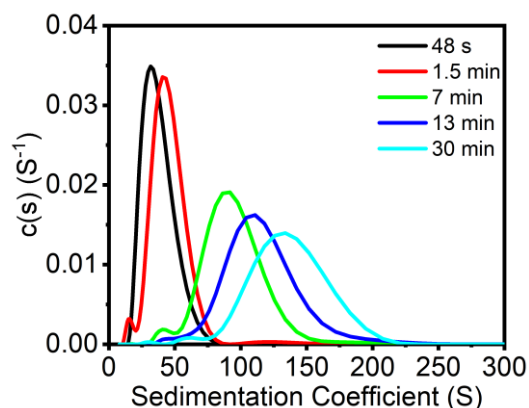


**Fig. 3.** Sedimentation coefficient distribution of InP aliquots at different reaction times.

While shape anisotropy cannot explain the observed discrepancy in the PSDs, the formation of agglomerates such as bipyramidal tetrahedrons is a reasonable explanation. Such particles could form after some time at 20 °C, which is why they might not be seen as clearly in STEM. Notably, there are studies reporting on the formation of duplets of tetrahedral particles [44-46]. For the UV-vis analysis, small agglomerates will not be seen as the primary particles will remain quantum confined. Another important observation for the AUC data is the existence of a shoulder in the sedimentation coefficient distributions, which is in the size range of the primary particles. Nevertheless, in order to resolve the herein reported ambiguities, extensive hydrodynamic modelling and further experimental studies are necessary to shed light on potential agglomeration phenomena. However, this is beyond the scope of this work and also not necessary for modelling the formation of the primary particles.

### 3.3 InP formation: Kinetics

UV-vis spectra were utilized as a fast and reliable footprint to track the formation of InP nanocrystals. To experimentally quantify the InP formation, the characteristic particle size ( $x_{mod}$ ) and solid concentration ( $c_s$ ) over time at different temperatures and initial [In] concentrations were collected. The former was discussed in the previous chapter, and the latter was calculated as described in the experimental section (Eq. (1)). Fig. 4 shows the evolution of the volume equivalent diameter ( $x_{mod}$ ) and the solid concentration ( $c_s$ ) of InP QDs synthesized at different temperatures and initial [In] concentrations. It can be seen that with increasing reaction temperature, the size of the produced particles and the solid concentration increase. As qualitatively discussed, the growth slows down over time until the reaction reaches equilibrium (Fig. 4a and 4b). Similarly, as shown in Fig. 4c, with an increase in the initial [In] concentration, the particles become smaller within a certain concentration range which results from more nuclei

being formed at higher precursor concentration due to the higher built-up of supersaturation in the solution. When the initial [In] concentration was as low as 0.035 M, there were only few particles forming which leads to inaccurate concentration-sensitive UV-vis measurements and PSD derivation. Therefore, for the low [In] concentration of 0.035 M, the kinetic data of  $x_{\text{mod}}$  over time will not be taken into account. Likewise, at this concentration, the evolution of the solid concentration will also not be considered. At high [In] concentration (0.07 M and 0.105 M), shown in Fig. 4d, the solid concentration increases with increasing initial [In] concentration. While the chemical yield kept almost constant with acceptable fluctuation which is consistent with the previous report of Buffard et al. [23] (Fig. S4).

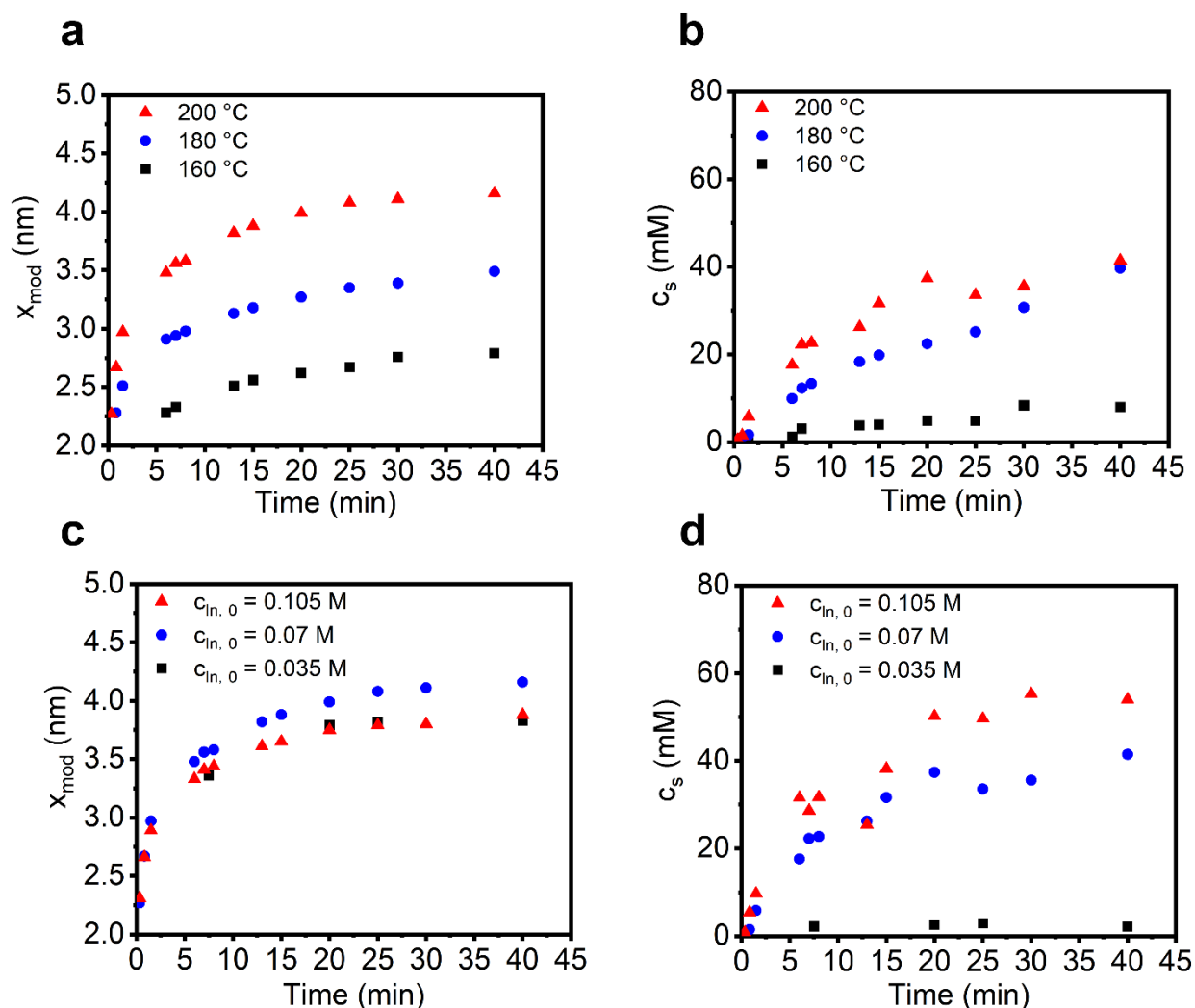


**Fig. 4.** Evolution of volume equivalent size ( $x_{\text{mod}}$ ) and solid concentration ( $c_s$ ) of InP QDs synthesized at (a, b) different temperatures and (c, d) initial [In] concentrations for population balance model development.

### 3.4 Modelling of InP formation

#### 3.4.1 Population balance model

The method of population balance equations is widely used to simulate crystallization and precipitation processes for particles from the micro to the nanometer range. The previously shown experimentally derived time resolved data was our starting point to derive the model equation for the simulation of the InP QD formation. The experimental data were fitted to the model equations and the fitted parameters were extracted and further validated by the comparison between the experimental results and simulation results.

As shown in Fig. 4 and Fig. S4, the temporal evolution of the mode particle size, the solid concentration, and the chemical yield change with the reaction temperature, which was also observed in previous studies [12, 23]. Recent studies [47, 48] showed that the solid formation of QDs is initially determined by the nucleation of clusters (nuclei) followed by molecular growth of free monomers attaching to the surface of the particles or nuclei. Prior solid formation commences, the precursor molecules react to monomer building blocks. As mentioned, the solution chemistry and the reaction mechanism are still under debate [25, 28]. To account for a yield change with the initial concentration and temperature, based on the work of Hens et al. [26], we propose a competitive by-product reaction of the phosphorous precursor complex as



Where  $A$  represents the phosphorous precursor and  $BP$  the product of a, here hypothesized, competing side reaction. The ratio  $R_k = \log_{10} \left( \frac{k_2}{k_1} \right)$  between the two reaction constants determines the concentration of free phosphorus monomers ( $P^{3-}$ ) and thus, the overall yield of the generated QDs. At this point it has to be mentioned that we had to introduce the competing reaction system because the existence of such a system is the only one capable of describing the experimentally observed phenomena such as the temperature dependent yield in the form of a global kinetics. We see this as central advantage of our approach as the need to match numerical with experimental data allows us to better understand the rate determining steps during InP QD formation. The free phosphorous monomer  $P^{3-}$  further reacts with the free indium monomer  $In^{3+}$  to the monomer building unit InP.



Because the time scale of the QD formation is in the range of minutes and a rigorous stirring of the precursor solution is applied, the influence of mixing on the QD formation is assumed to

have a negligible effect on the particle formation and is thus neglected [15]. The spatiotemporal evolution of the dispersed phase is modeled by a population balance equation (PBE) as

$$\dot{q}(t, x) + \left( G(c(t), x)q(t, x) \right)_x = 0, \quad (3)$$

where  $q$ ,  $x$  and  $c$  denote the number density function, the particle diameter and the free InP concentration in solution, respectively. The growth rate is given by  $G$ , the nucleation rate by  $N$  and  $x_{\text{nucl}}$  being the size of the nuclei. We assume that the molecular growth is reaction-limited, which implies that transport processes from the bulk to the particle surface are much faster than the integration of building units into the particle lattice. The growth rate reads as

$$G(c) = \begin{cases} k_g(c - c_{eq}) & \text{for } c > c_{eq} \\ 0 & \text{else} \end{cases} \quad (4)$$

where  $k_g$  is growth rate constant and  $c_{eq}$  is the equilibrium solubility of InP in solution. Note that, for reaction-limited growth, the growth rate describing the change of the particle radius or diameter is independent on the particle size [11]. The formation of new nuclei with the critical diameter  $x_{\text{nucl}}$  is prescribed in the PBE by a nucleation boundary condition [49] as

$$q(x_{\text{nucl}}, t) = \frac{N(c(t))}{G(c(t))}. \quad (5)$$

We here rely on the classical nucleation theory (CNT) to describe the nucleation rate  $N(c)$ . Especially, we apply the nucleation rate model of Mersmann [50-52]

$$N(c) = \begin{cases} C_{n1} S(c)^{\frac{7}{3}} \exp(-C_{n2} \log(S(c))^{-2}), & \text{for } S(c) > 1 \\ 0 & \text{else} \end{cases} \quad (6)$$

which has been successfully applied to many different chemical systems [53, 54]. Nucleation and growth only proceed if the system is supersaturated ( $S(c) > 1$ ), whereby the supersaturation  $S$  is quantified as

$$S(c) = \frac{c}{c_{eq}}. \quad (7)$$

The constants  $C_{n1}$  and  $C_{n2}$  in Eq. (6) read as

$$C_{n1} = \frac{3}{2} D_{sf} V_m \sqrt{\frac{\sigma}{k_b T}} (c_{eq} N_A)^{7/3} \quad \text{and} \quad C_{n2} = \frac{16}{3} \pi \frac{V_m^2 \sigma^3}{k_b^3 T^3}. \quad (8)$$

The material constants in  $C_{n1}$  and  $C_{n2}$  are known except for the equilibrium solubility  $c_{eq}$  and the surface energy  $\sigma$ , which will be estimated by a parameter study / optimization approach in the next section.

To complement the model, the PBE (Eq. (3) and (5)) is finally coupled with a mass balance to the concentration of InP

$$c(t) = c_{in}(t) - \frac{\pi \rho_p}{6 M_p} \int_{x_{nucl}}^{\infty} x^3 q(x, t) dx, \quad (9)$$

where  $c_{in}(t)$  accounts for the formation of InP units through the reaction in Eq. (2) [26]. This system was -- as proposed in [49] -- reformulated purely as an integral equation in the concentrations. Following the ideas presented in [49], this integral equation is then numerically approximated and, based on the solution formula presented in [49, 55], the full PSD information is obtained. This approach allowed to benefit on the one hand on the efficiency of PBE solution methods based on moments and on the other hand to have access to the full PSD.

### 3.4.2 Simulations

In the following, we seek to quantitatively model the QD formation with the proposed model. To do so, five unknown variables, namely the reaction ratio  $R_k$ , the reaction constant  $k_3$ , the surface energy  $\sigma$ , the equilibrium solubility  $c_{eq}$  and the growth rate constant  $k_g$ , need to be estimated. We here employ a rigorous optimization approach taking into account the experimental results from Fig. 4. More precisely, we calculate a cost function  $J$  with the relative squared Euclidean distance between simulation results and experimental results for the temporal evolution of the solid concentration  $c_s$ , the evolution of the mean particle size  $x_{1,3}$  and the full mass-weighted particle size distribution  $q_3$  after the process has finished.

$$J_c := \frac{\|c_{s,exp} - c_{s,sim}\|_{L^2((0,T))}^2}{\|c_{s,exp}\|_{L^2((0,T))}^2} = \frac{\int_0^T (c_{s,exp}(\tau) - c_{s,sim}(\tau))^2 d\tau}{\int_0^T (c_{s,exp}(\tau))^2 d\tau},$$

$$J_x := \frac{\|x_{1,3,exp} - x_{1,3,sim}\|_{L^2((0,T))}^2}{\|x_{1,3,exp}\|_{L^2((0,T))}^2}, \quad J_q := \frac{\|q_{3,exp}(T, \cdot) - q_{3,sim}(T, \cdot)\|_{L^2((x_n, \infty))}^2}{\|q_{3,exp}(T, \cdot)\|_{L^2((x_n, \infty))}^2} \quad (10)$$

which are by weighing factors  $\omega_i$  combined to the objective functional

$$J = \omega_1 J_c + \omega_2 J_x + \omega_3 J_q \quad (11)$$

The functional  $J$  is minimized by a systematic parameter study and a subsequent surrogate model-based optimization algorithm in order to obtain parameters to match the experimental data. The parameter space has 5 dimensions  $\mathbb{R}^5$ , i.e., the parameter space for each unknown is equidistantly divided into  $N_p$  parts, which requires to simulate the PBE model for  $N_p^5$  parameter sets. We herein set  $N_p = 18$  resulting in approximately 2 million of PBE simulations to be performed. These simulations were performed within approximately 30 h in parallel on a compute server using 30 cores with 2.4Ghz each. For each parameter set, at first the Euclidean distance for each quantity ( $c_s$ ,  $x_{1,3}$  and  $q_3$ ) is evaluated as cost functional. Afterwards, a statistical analysis is performed. In a second step, worse parameter combinations (large cost function values) are

excluded, and the parameter space is narrowed. The procedure was repeated three times. Finally, a derivative free optimization was performed based on a surrogate model (for this we have used the MATLAB inbuilt routine *surrogateopt*) which uses the previously identified parameter sets as starting information.

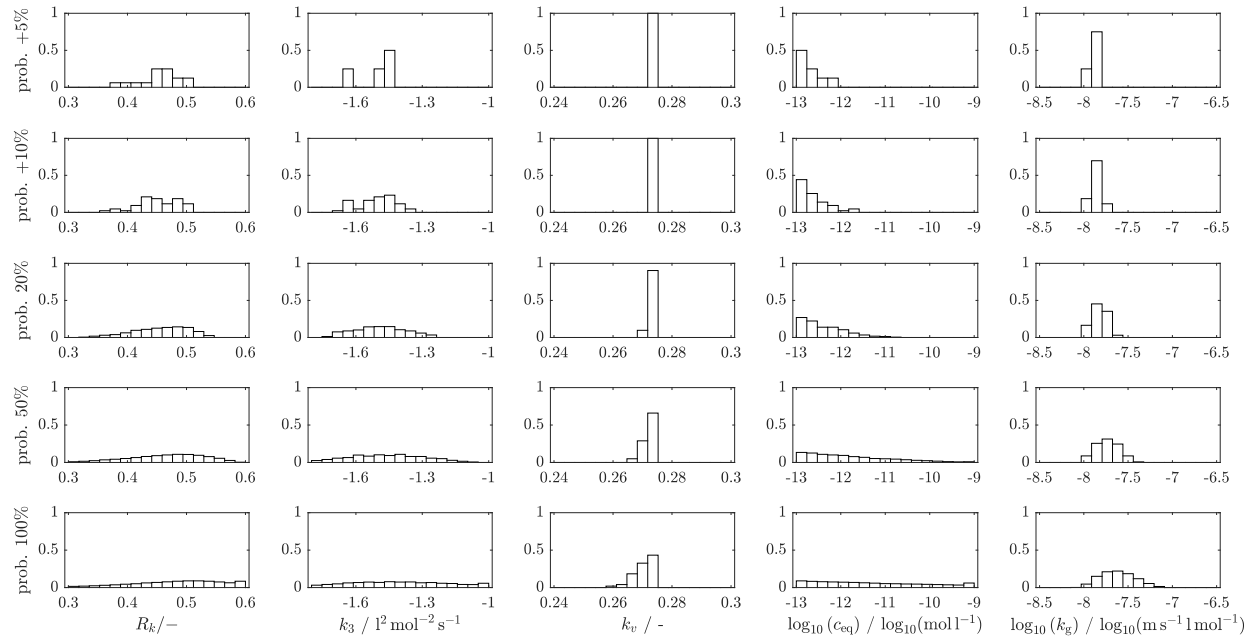


**Fig. 5.** Histograms showing the distributions of parameters rendering in a PBE solution with a relative L2-distance to the experimental data of at most 5 %, 10 %, 20 %, 50 % and 100 % (from top row to bottom row) more than the relative L2-distance of the best fitting parameters. (From left to right) unknown variables: yield determining ratio  $R_k$  of the precursor reaction constants,  $k_3$  reaction constant of  $3^{rd}$  reaction, Mersmann coefficient  $k_v$  correlating interfacial energy  $\sigma$  and solubility  $c_{eq}$ , solubility  $c_{eq}$  and growth rate constant  $k_g$ .

At first, we consider the experimental data for different initial concentrations at constant temperature ( $T=200$  °C) (shown in Fig. 4). In Fig. 5, the statistical analysis of the optimization is depicted. From left to right, the different unknown variables (the ratio  $R_k$ , the reaction constant  $k_3$ , the Mersmann coefficient  $k_v$  [56], the equilibrium solubility  $c_{eq}$  and the growth rate constant  $k_g$ ) are shown. The Mersmann coefficient  $k_v$  relates the equilibrium solubility  $c_{eq}$  with the surface energy  $\sigma$

$$\sigma = k_v \frac{k_b T}{V_m^{2/3}} \log \left( \frac{\rho_p}{M_p c_{eq}} \right). \quad (12)$$

For inorganic salts, the Mersmann coefficient takes a value of  $k_v = 0.31 \pm 200$  % [56]. Using the  $k_v$  in the optimization is of advantage because it determines the prevailing nucleation kinetics for

a given supersaturation level and limits the reasonable parameter space. Furthermore, in Fig. 5, histograms of the cost function for different relative error values are shown. As the percentage value is decreased, we obtain distinct optimal values for the reaction constant  $k_3$ , the Mersmann coefficient  $k_v$  and the growth rate constant  $k_g$ . For the reaction ratio  $R_k$  for the phosphorus by-product reaction, the solution space is narrow, but a clear optimum is not obtained. The reaction ratio  $R_k$  determines the final yield. For example, a yield of 50 % implies a value of  $R_k = 0.5$ . The quantitative comparison of the simulation results with the experimental results for the finally derived optimal parameter set is shown in Fig. 6. The experimental variance in the temporal evolution of the solid concentration  $c_s$  (see Fig. 6a) does not allow to find a distinct optimum, because the yield for both initial concentrations are not the same. The range of  $R_k = [0.4, 0.6]$  is a compromise between the relative square Euclidean distance of the two initial concentrations. It is noteworthy that – in line with our previous findings on ZnO QDs [57] - the optimal value of the equilibrium solubility  $c_{eq}$  appears to be below the assumed minimal value for the solubility of  $c_{eq} = 10^{-13}$  mol/L.

In a further step, the parameter space shown in Fig. 5 is used as starting point to find an optimal parameter set with the gradient free optimizer *surrogateopt*. The obtained parameters are listed in Table 1. With the optimal parameter set, we obtain very good quantitative agreement in the temporal evolution of the solid concentration, the mean particle size and the particle size distribution as seen in Fig. 6. We want to emphasize that the uniqueness of each parameter is not necessarily given by each of the three cost functions  $J_c$ ,  $J_x$  and  $J_q$  individually. For example, the temporal evolution of the solid concentration (see Fig. 4) is largely determined (even limited) by the reaction rate  $k_3$  of the InP reaction and the reaction ratio  $R_k$ . In contrast, the equilibrium solubility  $c_{eq}$ , the Mersmann coefficient  $k_v$  and the growth rate constant  $k_g$  largely influence the temporal evolution of the mean particle size and the full particle size distribution.

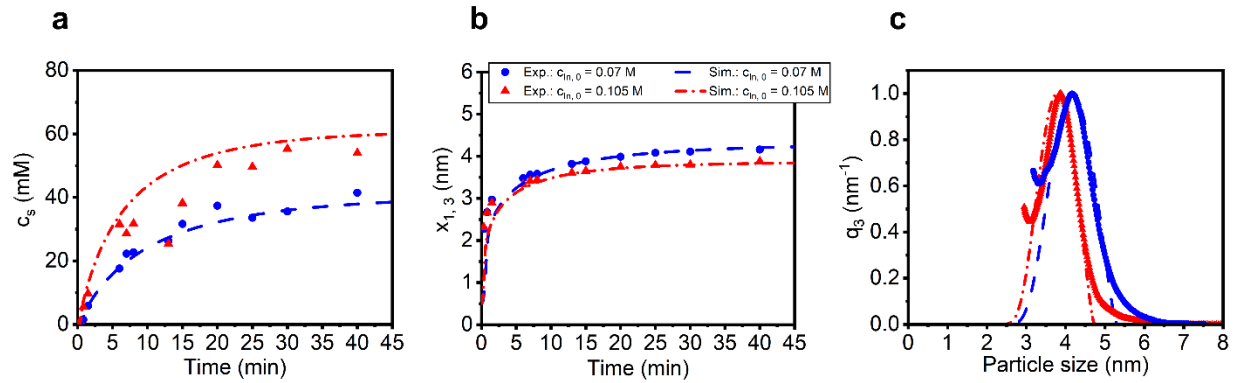


**Fig. 6.** a) Solid concentration  $c_s$  over time at  $T = 200\text{ }^\circ\text{C}$  for different initial Indium  $c_{In,0}$  and phosphorus concentrations  $c_{P,0}$ ; b) mean particle size  $x_{1,3}$  over time at  $T = 200\text{ }^\circ\text{C}$  for different initial Indium  $c_{In,0}$  and phosphorus concentrations  $c_{P,0}$ ; c) mass-weighted particle size distribution at  $t = 40\text{ min}$  for different initial indium concentrations  $c_{In,0}$  and phosphorus concentrations  $c_{P,0}$ . The legend in b) refers to all sub figures.

The ratio between initial indium concentration the initial phosphorus concentration is constant

$$(c_{In,0} / c_{P,0} = 1/2).$$

**Table 1.** Finally obtained optimal parameter values for the formation of InP QDs.

Parameter	$R_k / -$	$k_3 / \text{l}^2\text{mol}^{-2}\text{s}^{-1}$	$k_v / -$	$c_{eq} / \text{mol l}^{-1}$	$k_g / \text{m s}^{-1} \text{l mol}^{-1}$
Optimal value	0.3882	$10^{-1.565}$	0.263	$10^{-13}$	$10^{-7.588}$

### 3.4.3 Validation

For validation, we extend the modelling study and take into account the temperature influence on the QD synthesis (experimental results are shown in Fig .4). Except for the Mersmann coefficient  $k_v$ , a temperature dependence for the unknown parameters is to be expected. However, instead of prescribing a particular thermodynamic law to account for the temperature dependence, we let the optimizer run for the different temperatures ( $T = 160\text{ }^\circ\text{C}$  and  $T = 180\text{ }^\circ\text{C}$ ) with the optimized parameter set at  $T = 200\text{ }^\circ\text{C}$  as initial condition and afterwards deduce appropriate correlations between the resulting optimized parameter sets and the temperature. For the optimized parameter sets, an expectedly good agreement between experiments and simulations was obtained (Fig. 7). However, not only the temporal evolution of the solid concentration (Fig. 7a) and the mean particle size matched very well (Fig. 7b) but also the full particle size distribution of the final dispersion (Fig. 7c). Two findings are however remarkable. First, an Arrhenius type law  $k \propto \exp(-\frac{E_A}{RT})$  fits very well for all reaction rates  $k_i$  (Fig. 7d-7f) as well as for the growth rate constant  $k_g$ . The identified activation energies  $E_A$  for the InP reaction of  $28.5\text{ kJ/mol}$  and for the growth rate constant of  $57.4\text{ kJ/mol}$  are in remarkably good agreement

with literature, i.e. for the growth of InP, an activation energy of  $65.7 \pm 6.2$  kJ/mol is reported in [43], and for the ripening of ZnO QDs, an activation energy of 119 kJ/mol is found in [57]. This is a strong indication that the mechanisms of liquid phase reactions, nucleation and integration limited growth described in Section 3.4.1., reflect well the dominating dynamics. Second, the temperature dependence of the equilibrium solubility appears to be negligibly small. The temperature effect on the nucleation rate is given by the explicit temperature dependence of the attachment frequency and the Gibbs free energy. Note that usually the nucleation rate is derived under isothermal conditions such that the impact of pressure fluctuations and entropy changes are neglected, which applies also to the herein used nucleation rate. In this case, the temperature dependence of the Gibbs free energy stems from the chemical potential alone. For the sake of simplicity, we neglect the possible influence of pressure and entropy changes on the nucleation rate. Furthermore, the linear dependence of the surface energy on temperature given by the Mersmann correlation function (Eq. 12) is taken into account.

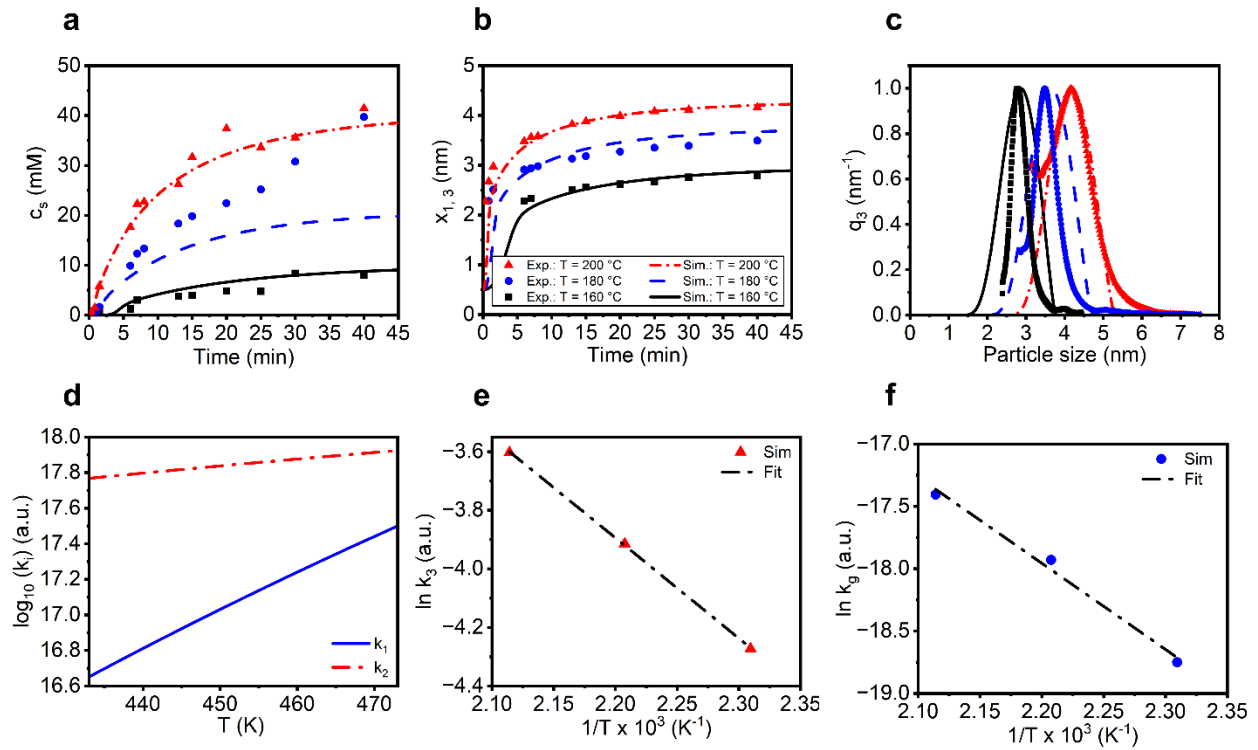


**Fig. 7.** a) Solid concentration  $c_s$  over time  $t$  for different temperatures  $T$  at  $c_{p,0} = 70$  mM and  $c_{In,0} = 140$  mM; b) mean particle size  $x_{1,3}$  over time  $t$  for different temperatures  $T$  at  $c_{p,0} = 70$  mM and  $c_{In,0} = 140$  mM; c) mass-weighted particle size distribution at  $t = 40$  min for different temperatures; d) temperature-dependent by-product reaction rates as a function of temperature  $T$ ; e) InP reaction rate  $k_3$  as a function of temperature  $T$ ; f) growth rate constant  $k_g$  as a function of temperature  $T$ . The legend in c) refers to all sub figures.

## 4 Conclusion

In this work, a global model based on population balance equations and experimental data has been proposed to describe the formation of InP QDs. In the experimental study, the synthesis of InP QDs using aminophosphine as a promising alternative to pyrophoric and toxic  $P(TMS)_3$ , was performed in an automated robotic platform, which enables accurate feeding and sampling and largely excludes human error [15]. The as-synthesized QDs exhibit the commonly-seen zinc blende crystal structure of InP and more importantly, high reproducibility. The shape of the as-synthesized InP QDs was found to be tetrahedral, especially in the later stages of the reaction. However, we were able to perform this study without introducing a shape factor by considering the equivalent sphere of the semiconducting volume. In line with our findings on PbS and PbSe [33] and literature data on InP from Kim et al. [42], the concept of volume equivalent diameters was found to be applicable to interpret the particle size derived from the UV-vis spectra. For the modelling, the reaction kinetics (temporal evolution of particle size distribution, mean particle size, solid concentration at different temperatures and concentrations) were recorded by UV-vis spectrometry. The temporal evolution of the solid concentration, i.e., the chemical yield, showed the expected yield change in dependence of the initial concentration and the temperature, suggesting a competitive by-product formation in the reaction scheme. The proposed model to describe the experimental data was fitted for unknown parameters (the reaction ratio  $R_k$ , the reaction constant  $k_3$ , the surface energy  $\sigma$ , the equilibrium solubility  $c_{eq}$  and the growth rate constant  $k_g$ ) by a rigorous optimization approach. The effect of temperature on the formation of InP was also experimentally and numerically studied. With the optimized parameter set, a very good agreement between the experimental results and the simulations was obtained. Remarkably, an Arrhenius type law fits very well for all reaction rates as well as for the growth rate constant and activation energies of 28.5 kJ/mol and 57.4 kJ/mol for the InP reaction rate and the growth rate constant respectively have been determined. These suggest the high potential of the proposed model to predict the evolution of InP QDs during nucleation and growth.

Overall, the developed strategy and therewith derived model represents a first step towards a more refined model to include, amongst others, shape factors, crystal structure and ligand binding kinetics. Additionally, the formation of agglomerates observed by AUC analysis needs to be investigated in more detail. Large-scale hydrodynamic modelling is targeted to get closer insights into the structure formation of particles that emerge during their synthesis and subsequent agglomeration.

## Acknowledgements

The authors are thankful for the funding of the Collaborative Research Centre 1411 “Design of Particulate Products” (Project-ID 416229255) and the research training group GRK1896 “In situ Microscopy with Electrons, X-rays and Scanning Probes” (Project-ID: 218975129) provided by Deutsche Forschungsgemeinschaft (DFG, German Research Foundation).

## Conflict of interest

There are no conflicts to declare.

## Note

Z. Wang, N. Traoré and T. Schikarski contributed equally to this work.

## References

- [1] A.L. Efros, L.E. Brus, Nanocrystal Quantum Dots: From Discovery to Modern Development, *Acs Nano* 15(4) (2021) 6192-6210. <https://doi.org/10.1021/acsnano.1c01399>.
- [2] Y.F. Shu, X. Lin, H.Y. Qin, Z. Hu, Y.Z. Jin, X.G. Peng, Quantum Dots for Display Applications, *Angew Chem Int Edit* 59(50) (2020) 22312-22323. <https://doi.org/10.1002/anie.202004857>.
- [3] Y.H. Won, O. Cho, T. Kim, D.Y. Chung, T. Kim, H. Chung, H. Jang, J. Lee, D. Kim, E. Jang, Highly efficient and stable InP/ZnSe/ZnS quantum dot light-emitting diodes, *Nature* 575(7784) (2019) 634-+. <https://doi.org/10.1038/s41586-019-1771-5>.
- [4] Q. Zhao, R. Han, A.R. Marshall, S. Wang, B.M. Wieliczka, J. Ni, J.J. Zhang, J.Y. Yuan, J.M. Luther, A. Hazarika, G.R. Li, Colloidal Quantum Dot Solar Cells: Progressive Deposition Techniques and Future Prospects on Large-Area Fabrication, *Adv Mater* 34(17) (2022). <https://doi.org/ARTN> 2107888  
10.1002/adma.202107888.
- [5] I. Gur, N.A. Fromer, M.L. Geier, A.P. Alivisatos, Air-stable all-inorganic nanocrystal solar cells processed from solution, *Science* 310(5747) (2005) 462-465. <https://doi.org/10.1126/science.1117908>.
- [6] G.S. Hong, A.L. Antaris, H.J. Dai, Near-infrared fluorophores for biomedical imaging, *Nat Biomed Eng* 1(1) (2017). <https://doi.org/ARTN> 0010  
10.1038/s41551-016-0010.
- [7] F.P. Garcia de Arquer, D.V. Talapin, V.I. Klimov, Y. Arakawa, M. Bayer, E.H. Sargent, Semiconductor quantum dots: Technological progress and future challenges, *Science* 373(6555) (2021). <https://doi.org/10.1126/science.aaz8541>.
- [8] A.I. Ekimov, A.L. Efros, A.A. Onushchenko, Quantum Size Effect in Semiconductor Microcrystals, *Solid State Commun* 56(11) (1985) 921-924. <https://doi.org/Doi> 10.1016/S0038-1098(85)80025-9.

- [9] R. Rossetti, S. Nakahara, L.E. Brus, Quantum Size Effects in the Redox Potentials, Resonance Raman-Spectra, and Electronic-Spectra of Cds Crystallites in Aqueous-Solution, *J Chem Phys* 79(2) (1983) 1086-1088. <https://doi.org/Doi> 10.1063/1.445834.
- [10] P. Reiss, M. Protiere, L. Li, Core/Shell semiconductor nanocrystals, *Small* 5(2) (2009) 154-68. <https://doi.org/10.1002/sml.200800841>.
- [11] S. Tamang, C. Lincheneau, Y. Hermans, S. Jeong, P. Reiss, Chemistry of InP Nanocrystal Syntheses, *Chem Mater* 28(8) (2016) 2491-2506. <https://doi.org/10.1021/acs.chemmater.5b05044>.
- [12] M.D. Tessier, D. Dupont, K. De Nolf, J. De Roo, Z. Hens, Economic and Size-Tunable Synthesis of InP/ZnE (E = S, Se) Colloidal Quantum Dots, *Chem Mater* 27(13) (2015) 4893-4898. <https://doi.org/10.1021/acs.chemmater.5b02138>.
- [13] S. Kubendhiran, Z. Bao, K. Dave, R.S. Liu, Microfluidic Synthesis of Semiconducting Colloidal Quantum Dots and Their Applications, *Acs Appl Nano Mater* 2(4) (2019) 1773-1790. <https://doi.org/10.1021/acsnm.9b00456>.
- [14] D.S. Salley, G.A. Keenan, D.L. Long, N.L. Bell, L. Cronin, A Modular Programmable Inorganic Cluster Discovery Robot for the Discovery and Synthesis of Polyoxometalates, *Acs Central Sci* 6(9) (2020) 1587-1593. <https://doi.org/10.1021/acscentsci.0c00415>.
- [15] A.M. Salaheldin, J. Walter, P. Herre, I. Levchuk, Y. Jabbari, J.M. Kolle, C.J. Brabec, W. Peukert, D. Segets, Automated synthesis of quantum dot nanocrystals by hot injection: Mixing induced self-focusing, *Chem Eng J* 320 (2017) 232-243. <https://doi.org/10.1016/j.cej.2017.02.154>.
- [16] E.M. Chan, C.X. Xu, A.W. Mao, G. Han, J.S. Owen, B.E. Cohen, D.J. Milliron, Reproducible, High-Throughput Synthesis of Colloidal Nanocrystals for Optimization in Multidimensional Parameter Space, *Nano Lett* 10(5) (2010) 1874-1885. <https://doi.org/10.1021/nl100669s>.
- [17] A.S. Mahmoud, D. Segets, Cleaning Matters!, *Acs Comb Sci* 21(11) (2019) 722-725. <https://doi.org/10.1021/acscombsci.9b00122>.
- [18] J.S. Owen, E.M. Chan, H.T. Liu, A.P. Alivisatos, Precursor Conversion Kinetics and the Nucleation of Cadmium Selenide Nanocrystals, *J Am Chem Soc* 132(51) (2010) 18206-18213. <https://doi.org/10.1021/ja106777j>.
- [19] S. Abe, R.K. Capek, B. De Geyter, Z. Hens, Tuning the Postfocused Size of Colloidal Nanocrystals by the Reaction Rate: From Theory to Application, *Acs Nano* 6(1) (2012) 42-53. <https://doi.org/10.1021/nn204008q>.
- [20] T. Sugimoto, F. Shiba, Spontaneous nucleation of monodisperse silver halide particles from homogeneous gelatin solution II: silver bromide, *Colloid Surface A* 164(2-3) (2000) 205-215. <https://doi.org/Doi> 10.1016/S0927-7757(99)00365-9.
- [21] D. Franke, D.K. Harris, L. Xie, K.F. Jensen, M.G. Bawendi, The Unexpected Influence of Precursor Conversion Rate in the Synthesis of III-V Quantum Dots, *Angew Chem Int Ed Engl* 54(48) (2015) 14299-303. <https://doi.org/10.1002/anie.201505972>.
- [22] O.B. Achorn, D. Franke, M.G. Bawendi, Seedless Continuous Injection Synthesis of Indium Phosphide Quantum Dots as a Route to Large Size and Low Size Dispersity, *Chem Mater* 32(15) (2020) 6532-6539. <https://doi.org/10.1021/acs.chemmater.0c01906>.
- [23] A. Buffard, S. Dreyfuss, B. Nadal, H. Heuclin, X. Xu, G. Patriarche, N. Mézailles, B. Dubertret, Mechanistic Insight and Optimization of InP Nanocrystals Synthesized with Aminophosphines, *Chem Mater* 28(16) (2016) 5925-5934. <https://doi.org/10.1021/acs.chemmater.6b02456>.

- [24] V.K. Lamer, R.H. Dinegar, Theory, Production and Mechanism of Formation of Monodispersed Hydrosols, *J Am Chem Soc* 72(11) (1950) 4847-4854. <https://doi.org/DOI.10.1021/ja01167a001>.
- [25] B.M. McMurtry, K. Qan, J.K. Teglassi, A.K. Swarnakar, J. De Roo, J.S. Owen, Continuous Nucleation and Size Dependent Growth Kinetics of Indium Phosphide Nanocrystals, *Chem Mater* 32(10) (2020) 4358-4368. <https://doi.org/10.1021/acs.chemmater.0c01561>.
- [26] M.D. Tessier, K. De Nolf, D. Dupont, D. Sinnaeve, J. De Roo, Z. Hens, Aminophosphines: A Double Role in the Synthesis of Colloidal Indium Phosphide Quantum Dots, *J Am Chem Soc* 138(18) (2016) 5923-5929.
- [27] D.C. Gary, M.W. Terban, S.J.L. Billinge, B.M. Cossairt, Two-Step Nucleation and Growth of InP Quantum Dots via Magic-Sized Cluster Intermediates, *Chem Mater* 27(4) (2015) 1432-1441. <https://doi.org/10.1021/acs.chemmater.5b00286>.
- [28] Y. Kwon, S. Kim, Indium phosphide magic-sized clusters: chemistry and applications, *Npg Asia Mater* 13(1) (2021). <https://doi.org/ARTN.10.1038/s41427-021-00300-4>.
- [29] J. Walter, K. Lohr, E. Karabudak, W. Reis, J. Mikhael, W. Peukert, W. Wohlleben, H. Colfen, Multidimensional Analysis of Nanoparticles with Highly Disperse Properties Using Multiwavelength Analytical Ultracentrifugation, *Acs Nano* 8(9) (2014) 8871-8886. <https://doi.org/10.1021/nn503205k>.
- [30] J. Pearson, J. Walter, W. Peukert, H. Colfen, Advanced Multiwavelength Detection in Analytical Ultracentrifugation, *Anal Chem* 90(2) (2018) 1280-1291. <https://doi.org/10.1021/acs.analchem.7b04056>.
- [31] P. Schuck, M.A. Perugini, N.R. Gonzales, G.J. Howlett, D. Schubert, Size-distribution analysis of proteins by analytical ultracentrifugation: Strategies and application to model systems, *Biophys J* 82(2) (2002) 1096-1111. [https://doi.org/Doi.10.1016/S0006-3495\(02\)75469-6](https://doi.org/Doi.10.1016/S0006-3495(02)75469-6).
- [32] D. Segets, J. Gradl, R.K. Taylor, V. Vassilev, W. Peukert, Analysis of Optical Absorbance Spectra for the Determination of ZnO Nanoparticle Size Distribution, Solubility, and Surface Energy, *Acs Nano* 3(7) (2009) 1703-1710. <https://doi.org/10.1021/nn900223b>.
- [33] D. Segets, J.M. Lucas, R.N.K. Taylor, M. Scheele, H.M. Zheng, A.P. Alivisatos, W. Peukert, Determination of the Quantum Dot Band Gap Dependence on Particle Size from Optical Absorbance and Transmission Electron Microscopy Measurements, *Acs Nano* 6(10) (2012) 9021-9032. <https://doi.org/10.1021/nn303130d>.
- [34] A.A. Guzelian, J.E.B. Katari, A.V. Kadavanich, U. Banin, K. Hamad, E. Juban, A.P. Alivisatos, R.H. Wolters, C.C. Arnold, J.R. Heath, Synthesis of size-selected, surface-passivated InP nanocrystals, *J Phys Chem-US* 100(17) (1996) 7212-7219. <https://doi.org/DOI.10.1021/jp953719f>.
- [35] H.X. Fu, A. Zunger, InP quantum dots: Electronic structure, surface effects, and the redshifted emission, *Phys Rev B* 56(3) (1997) 1496-1508. <https://doi.org/DOI.10.1103/PhysRevB.56.1496>.
- [36] J.M. Ferreyra, C.R. Proetto, Quantum size effects on excitonic Coulomb and exchange energies in finite-barrier semiconductor quantum dots, *Phys Rev B* 60(15) (1999) 10672-10675. <https://doi.org/DOI.10.1103/PhysRevB.60.10672>.
- [37] H. Yu, J.B. Li, R.A. Loomis, L.W. Wang, W.E. Buhro, Two- versus three-dimensional quantum confinement in indium phosphide wires and dots, *Nat Mater* 2(8) (2003) 517-520. <https://doi.org/10.1038/nmat942>.

- [38] S. Baskoutas, A.F. Terzis, Size-dependent band gap of colloidal quantum dots, *J Appl Phys* 99(1) (2006). <https://doi.org/Artn> 013708  
10.1063/1.2158502.
- [39] M. Li, J.C. Li, Size effects on the band-gap of semiconductor compounds, *Mater Lett* 60(20) (2006) 2526-2529. <https://doi.org/10.1016/j.matlet.2006.01.032>.
- [40] E. Cho, H. Jang, J. Lee, E. Jang, Modeling on the size dependent properties of InP quantum dots: a hybrid functional study, *Nanotechnology* 24(21) (2013). <https://doi.org/Artn> 215201  
10.1088/0957-4484/24/21/215201.
- [41] M. Goyal, M. Singh, Size and shape dependence of optical properties of nanostructures, *Appl Phys a-Mater* 126(3) (2020). <https://doi.org/10.1007/s00339-020-3327-9>.
- [42] K. Kim, D. Yoo, H. Choi, S. Tamang, J.H. Ko, S. Kim, Y.H. Kim, S. Jeong, Halide-Amine Co-Passivated Indium Phosphide Colloidal Quantum Dots in Tetrahedral Shape, *Angew Chem Int Edit* 55(11) (2016) 3714-3718. <https://doi.org/10.1002/anie.201600289>.
- [43] Y. Kim, H. Choi, Y. Lee, W.K. Koh, E. Cho, T. Kim, H. Kim, Y.H. Kim, H.Y. Jeong, S. Jeong, Tailored growth of single-crystalline InP tetrapods, *Nature Communications* 12(1) (2021). <https://doi.org/ARTN> 4454  
10.1038/s41467-021-24765-7.
- [44] C. Shang, W. Hong, Y. Guo, J. Wang, E. Wang, Water-Based Synthesis of Palladium Trigonal Bipyramidal/Tetrahedral Nanocrystals with Enhanced Electrocatalytic Oxidation Activity, *Chem. Eur. J.* 23(24) (2017) 5799-5803. <https://doi.org/10.1002/chem.201700172>.
- [45] X. Huang, S. Tang, H. Zhang, Z. Zhou, N. Zheng, Controlled Formation of Concave Tetrahedral/Trigonal Bipyramidal Palladium Nanocrystals, *J. Am. Chem. Soc.* 131(39) (2009) 13916–13917.
- [46] Y. Nagaoka, R. Tan, R. Li, H. Zhu, D. Eggert, Y.A. Wu, Y. Liu, Z. Wang, O. Chen, Superstructures generated from truncated tetrahedral quantum dots, *Nature* 561(7723) (2018) 378-382. <https://doi.org/10.1038/s41586-018-0512-5>.
- [47] S.G. Kwon, T. Hyeon, Formation Mechanisms of Uniform Nanocrystals via Hot-Injection and Heat-Up Methods, *Small* 7(19) (2011) 2685-2702. <https://doi.org/10.1002/sml.201002022>.
- [48] J. van Embden, A.S.R. Chesman, J.J. Jasieniak, The Heat-Up Synthesis of Colloidal Nanocrystals, *Chem Mater* 27(7) (2015) 2246-2285. <https://doi.org/10.1021/cm5028964>.
- [49] L. Pflug, T. Schikarski, A. Keimer, W. Peukert, M. Stingl, eMoM: Exact method of moments-Nucleation and size dependent growth of nanoparticles, *Comput Chem Eng* 136 (2020). <https://doi.org/ARTN> 106775  
10.1016/j.compchemeng.2020.106775.
- [50] A. Mersmann, K. Bartosch, How to predict the metastable zone width, *J Cryst Growth* 183(1-2) (1998) 240-250. <https://doi.org/Doi> 10.1016/S0022-0248(97)00417-X.
- [51] T. Schikarski, M. Avila, W. Peukert, En route towards a comprehensive dimensionless representation of precipitation processes, *Chem Eng J* 428 (2022). <https://doi.org/ARTN> 131984  
10.1016/j.cej.2021.131984.
- [52] T. Schikarski, M. Avila, H. Trzenschiok, A. Gueldenpfennig, W. Peukert, Quantitative modeling of precipitation processes, *Chem Eng J* 444 (2022). <https://doi.org/ARTN> 136195

10.1016/j.cej.2022.136195.

[53] X.J. Liu, Y. Huang, X.X. Li, J.X. Liu, Kinetics of crystal growth of glycine manganese chloride in aqueous supersaturated solutions, *Optik* 164 (2018) 443-448. <https://doi.org/10.1016/j.ijleo.2018.03.050>.

[54] L.D. Shiau, Investigations into the Influence of Solvents on the Nucleation Kinetics for Isonicotinamide, Lovastatin, and Phenacetin, *Acs Omega* 4(17) (2019) 17352-17358. <https://doi.org/10.1021/acsomega.9b02102>.

[55] A. Keimer, L. Pflug, M. Spinola, Nonlocal Scalar Conservation Laws on Bounded Domains and Applications in Traffic Flow, *Siam J Math Anal* 50(6) (2018) 6271-6306. <https://doi.org/10.1137/18m119817x>.

[56] A. Mersmann, Calculation of Interfacial-Tensions, *J Cryst Growth* 102(4) (1990) 841-847. <https://doi.org/Doi> 10.1016/0022-0248(90)90850-K.

[57] M. Haderlein, D. Segets, M. Groschel, L. Pflug, G. Leugering, W. Peukert, FIMOR: An efficient simulation for ZnO quantum dot ripening applied to the optimization of nanoparticle synthesis, *Chem Eng J* 260 (2015) 706-715. <https://doi.org/10.1016/j.cej.2014.09.040>.

## Supporting information

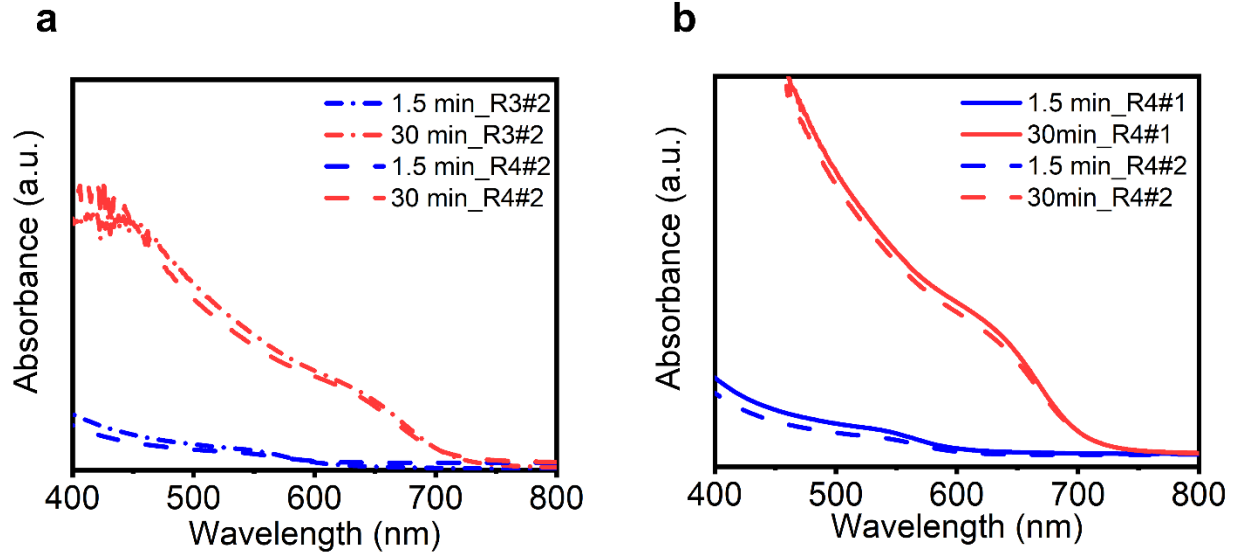


**Fig. S1.** Reproducibility in a) different reactors and b) at different times.

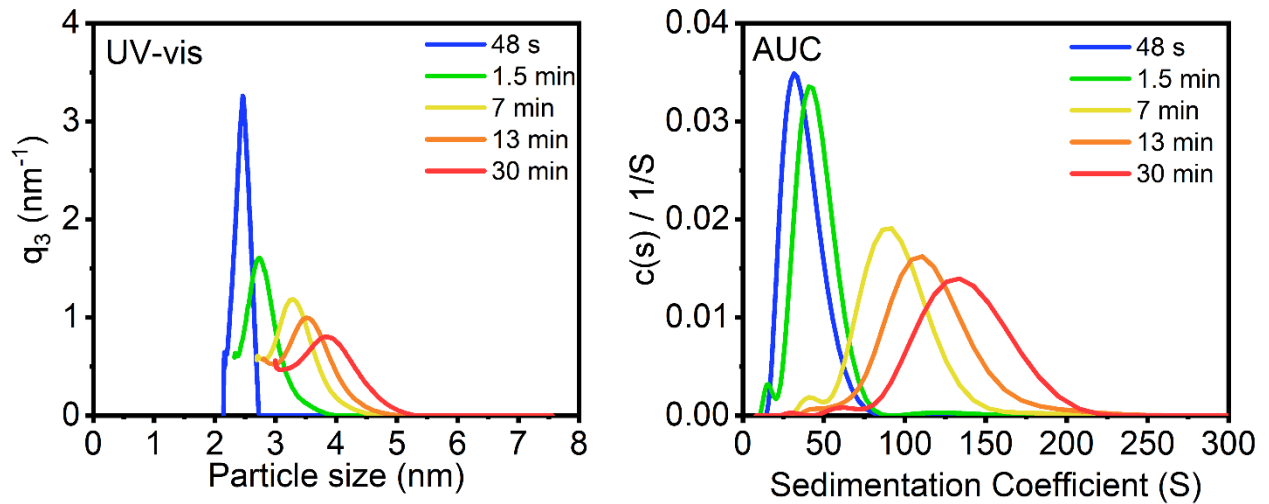


**Fig. S2.** Particle size distributions derived from UV-vis spectra and AUC data. For conversion to particle size, we assume a ligand shell thickness of 2.0 nm [Jörg Radnik, *et al. Analytical and Bioanalytical Chemistry* 414 (2022), 4331–4345] and a shell density of 0.736  $\text{g}/\text{cm}^3$  (50% oleylamine, 50 % n-hexane).

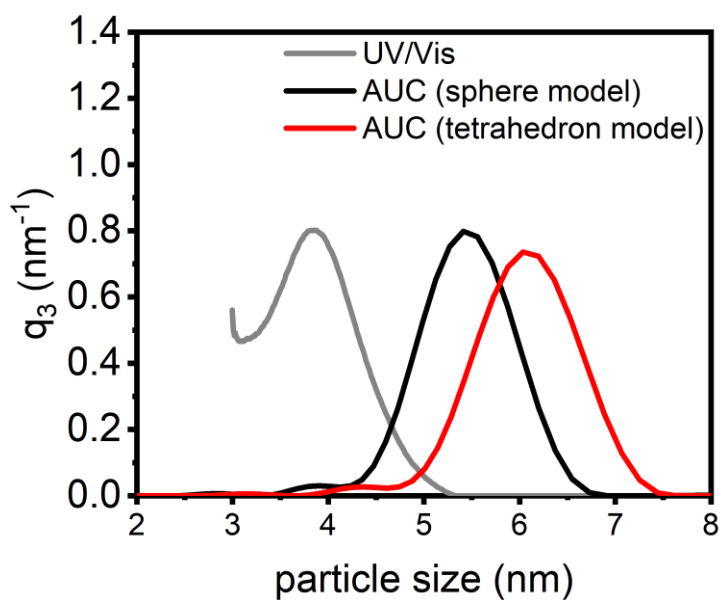


**Fig. S3.** Comparison of particle size distributions derived from UV-vis, AUC with spherical shape assumption and AUC with tetrahedral shape assumption. For the ligand shell, the same parameters are taken as for Fig. S2.

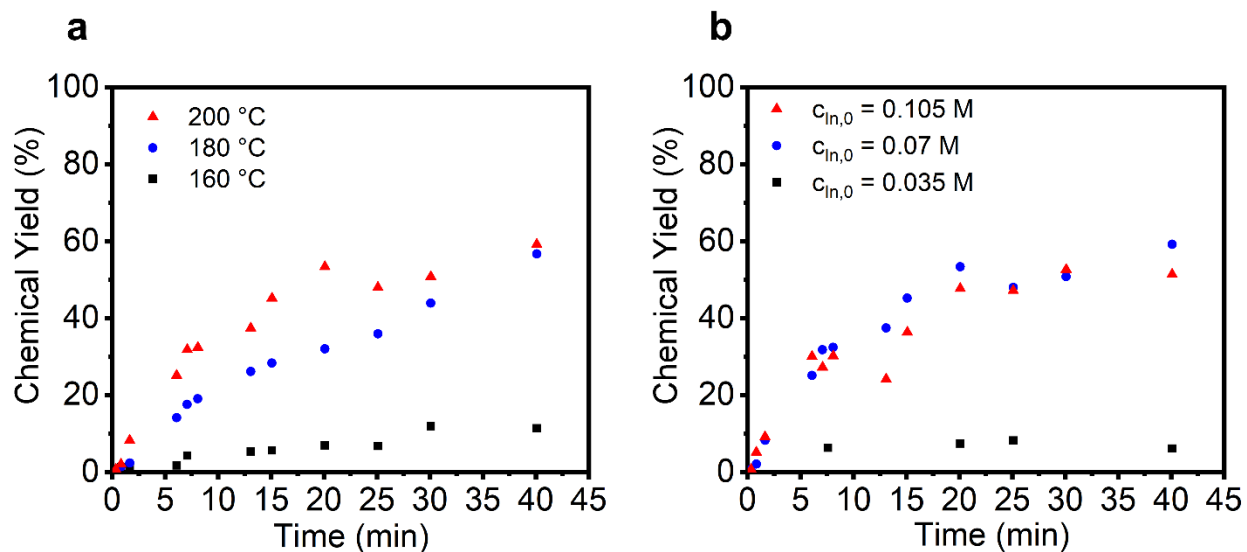
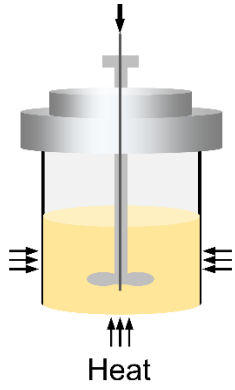


**Fig. S4.** Chemical yield at different a) temperatures and b) concentrations.

# Graphical abstract

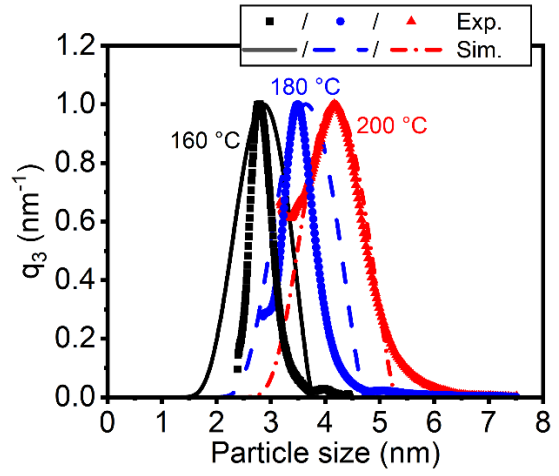
Robot feeding and sampling arm



Population balance modeling



Fitted parameters



## Highlights

1. An aminophosphine-based automated synthesis of InP QDs with high reproducibility was demonstrated.
2. PSDs derived from the UV-vis spectra can be interpreted as volume equivalent diameters in case of InP QDs with tetrahedral shape.
3. A predictive model based on population balance equation was proposed.
4. With the optimized parameter set, a very good agreement between experimental results and simulations was obtained, including activation energies.